Bacteria-like mesoporous silica-coated gold nanorods for positron emission tomography and photoacoustic imaging-guided chemo-photothermal combined therapy

Cheng Xu [a], Feng Chen [a], Hector F. Valdovinos [b], Dawei Jiang [a], Shreya Goel [c], Bo Yu [a], Haiyan Sun [a], Todd E. Barnhart [b], James J. Moon [d, e, f], Weibo Cai [a, b, c, g, *]

[a] Department of Radiology, University of Wisconsin–Madison, WI 53705, United States
[b] Department of Medical Physics, University of Wisconsin–Madison, WI 53705, United States
[c] Department of Materials Science and Engineering, University of Wisconsin–Madison, WI 53706, United States
[d] Department of Pharmaceutical Science, University of Michigan, Ann Arbor, MI 48109, United States
[e] Biointerfaces Institute, University of Michigan, Ann Arbor, MI 48109, United States
[f] Department of Biomedical Engineering, University of Michigan, Ann Arbor, MI 48109, United States
[g] University of Wisconsin Carbone Cancer Center, Madison, WI 53705, United States

ARTICLE INFO

ABSTRACT

Mesoporous silica nanoshell (MSN) coating has been demonstrated as a versatile surface modification strategy for various kinds of inorganic functional nanoparticles, such as gold nanorods (GNRs), to achieve not only improved nanoparticle stability but also concomitant drug loading capability. However, limited drug loading capacity and low tumor accumulation rate *in vivo* are two major challenges for the biomedical applications of MSN-coated GNRs (GNR@MSN). In this study, by coating uniformly sized GNRs with MSN in an oil-water biphase reaction system, we have successfully synthesized a new bacteria-like GNR@MSN (i.e., bGNR@MSN) with a significantly enlarged pore size (4–8 nm) and surface area (470 m^2/g). After PEGylation and highly efficient loading of doxorubicin (DOX, 40.9%, w/w), bGNR@MSN were used for positron emission tomography (PET, via facile and chelator-free ^{89}Zr-labeling) and photoacoustic imaging-guided chemo-photothermal cancer therapy *in vivo*. PET imaging showed that ^{89}Zr-labeled bGNR@MSN(DOX)-PEG can passively target to the 4T1 murine breast cancer-bearing mice with high efficiency (~10 %ID/g), based on enhanced permeability and retention effect. Significantly enhanced chemo-photothermal combination therapy was also achieved due to excellent photothermal effect and near-infrared-light-triggered drug release by bGNR@MSN(DOX)-PEG at the tumor site. The promising results indicate great potential of bGNR@MSN-PEG nanoplatforms for future cancer diagnosis and therapy.

© 2018 Elsevier Ltd. All rights reserved.

1. Introduction

Gold nanorods (GNRs), with anisotropic shape, tunable size, intrinsic biocompatibility and strong optical absorption at near-infrared (NIR) wavelength range are one of the most widely studied noble metal nanomaterials for potential biomedical applications [1–4], including but not limited to biomedical imaging [5,6], drug delivery [7–11], biomolecular sensing [12] and photothermal

therapy [8,13–16]. However, biomedical application of GNRs have been limited due to poor solubility, potential cytotoxicity from the residual surface surfactants [17] and suboptimal imaging and drug loading capacities [18,19]. Mesoporous silica nanoshell (MSN) with large surface area, tunable size and high pore volume has been widely used as a coating material for inorganic functional nanoparticles, including GNRs, to improve their *in vivo* stability and offer drug loading capability [20,21]. Photothermal therapy (PTT) has been developed as a promising strategy for cancer treatment [13–16] and other biomedical applications [22–24] which employ the heat generated from the light-absorbing agents accumulated in the tissue or tumor area. Some reports have demonstrated the applications of MSN coated-GNRs (GNR@MSN) for combining

---

photothermal therapy with chemotherapy (chemo-photothermal therapy) to achieve synergistic anticancer effects [10,13,25].

Nevertheless, the pore size and surface area of previously reported GNR@MSN are usually in the range of 0.5—4.0 nm and 50—350 m^2/g, respectively [4,13,25] which led to limited drug loading capacity and consequently suboptimal therapeutic outcomes. Large pore (>5 nm), biodegradable mesoporous silica nanoparticles with greater surface areas can be easily synthesized via a facile oil-water biphase stratification approach [26,27]. However, it's still a major challenge to coat uniform mesoporous silica layers with large pore size (>5 nm), high pore volume and surface area on the surface of GNRs and suited for *in vivo* biomedical applications [28]. In addition, previous reports have employed optical imaging or inductively coupled plasma mass spectrometry techniques to study the biodistribution of GNR@MSN *in vivo*, which yield partial information or are very invasive requiring many animals to be sacrificed [14,18]. Thus, more sensitive, non-invasive and dynamic imaging approaches are desirable for the systematic studies of *in vivo* pharmacokinetics of GNR@MSN.

Positron emission tomography (PET) is a highly sensitive and noninvasive radionuclide imaging method which can provide quantitative assessment of *in vivo* nanoparticles biodistribution and pharmacokinetics [29,30]. Photoacoustic (PA) imaging, with rich optical contrast, deep penetration and high ultrasonic spatial resolution, has received immense attention recently in the field of cancer diagnosis and therapy [31]. Combining PET with PA imaging could overcome the limitations of single modality and improve the diagnostic accuracy [32]. In addition, with one nanoplatform acting as both the contrast agent and therapeutic agent, specific imaging-guided cancer therapy can be easily realized [33].

In this study, we develop a novel strategy to fabricate GNR@MSN multifunctional nanoplatforms with a bacteria-like morphology. As developed bacteria-like GNR@MSN (bGNR@MSN) demonstrates large pore size, high pore volume and surface area, resulting in high doxorubicin (DOX) loading efficiency (40.9%, w/w). After PEGylation and chelator-free labeling with radioisotope zirconium-89 (^{89}Zr, $t_{1/2} = 78.4$ h) [34], PET and PA imaging-guided *in vivo* cancer therapy was subsequently conducted. The results showed chemo-photothermal cancer treatment mediated by bGNR@MSN(DOX)-PEG exhibited significantly enhanced therapeutic efficacy in 4T1 murine breast tumor-bearing mice.

2. Experimental

2.1. Reagents and materials

All reagents were analytical or higher grade. Gold (III) chloride solution (HAuCl$_4$·3H$_2$0), tetraethyl orthosilicate (TEOS), cetyl-trimethylammonium bromide (CTAB), cetyltrimethylammonium chloride (CTAC), AgNO$_3$, NaBH$_4$, L-ascorbic acid, oleic acid, [3-(4,5-dimethylthiazol-2-yl)-3,5-diphenytetrazolium bromide] (MTT), (3-mercatopropyl)trimethoxy-silane (MPTMS), (3-aminopropyl) triethoxysilane (APS), triethylamine (TEA) and Chelex 100 resin (50—100 mesh) were purchased from Sigma-Aldrich (St. Louis, MO). Succinimidyl carboxymethyl PEG maleimide (SCM-PEG-Mal; molecular weight: 5 kDa) was purchased from Creative PEGworks (Winston Salem, NC). All buffers and water were Millipore grade and pre-treated with Chelex 100 to remove heavy metal. All other reaction chemicals and reagent were purchased from Thermo Fisher Scientific (Fair Lawn, NJ).

2.2. Characterization

Transmission electron microscopy (TEM) images were obtained by Tecnai TF-30, 300 kV field emission. Nitrogen adsorption-desorption isotherms were measured at 77.3 K using a Quantachrome NovaWin2 system. Surface areas and pore size were determined by the BET (Barrett-Joyner-Halenda) method. Size and zeta analysis were performed on Nano-ZS90 Zetasizer (Malvern Instruments Ltd.). UV—vis spectra were recorded on Agilent Cary 60 spectrophotometer. Photothermal images were recorded by a FLIR™ E50 camera.

2.3. Synthesis of GNRs and bGNR@MSN-PEG

GNRs were synthesized according to the seed-mediated growth method [35] with the surfactant CTAC and oleic acid (see Supporting Information). Mesoporous silica layers were coated on the surface of GNRs by an oil-water biphase reaction approach [26]. In a typical process, 10 mL of CTAC solution (25 wt%), 10 mL GNRs water solution (0.2 mg/mL) and 0.1 g of TEA were added to 36 mL of water and stirred gently at 60 °C for 1 h in a 100 mL round-bottom flask. 10 μL of 1 mM MPTMS ethanol solution was added. Then ten milliliters of (5% v/v) TEOS in cyclohexane was carefully added to the CTAC-TEA aqueous solution and kept at 60 °C in a water bath for 12 h. Afterward, bGNR@MSN were collected by centrifugation (at 9000 rpm for 10 min). The precipitates were re-dispersed and washed by 1 wt % NaCl/methanol solution to remove CTAC for five times (24 h/time).

Surface amino modification was achieved by adding 1 mL of APS to 10 mL of bGNR@MSN in absolute ethanol solution. The mixture was kept in 35 °C water bath and stirred for 72 h, followed by repeated centrifugation and washing with ethanol to remove any unreacted APS. bGNR@MSN-NH$_2$ was then dispersed in water, 5 mg SCM-PEG$_{5k}$-Mal was added to the solution and reacted for 2 h. Finally, bGNR@MSN-PEG were collected by centrifugation (9000 rpm for 10 min) and washed with water for 3 times to remove excess PEG.

2.4. Photothermal effect of bGNR@MSN and DOX loading and release

Different concentrations of bGNR@MSN in water solution were irradiated by a NIR laser (808 nm, 0.25 W/cm^2) for 10 min and cooled down for another 10 min. The temperature of the solution was recorded by using a digital thermometer. Pure mesoporous silica nanoparticles (MSNs) solution (3 mg/mL) and water were used as controls.

DOX was loaded into bGNR@MSN-PEG by mixing the drug with bGNR@MSN-PEG in a PBS buffer at different pH values (5.3 and 7.4) for 24 h, and unloaded DOX was removed with the supernatant after centrifugation (9000 rpm for 10 min). The precipitates were washed by PBS until the supernatant became colorless. The DOX concentration in all supernatants was recorded to calculate the drug loading efficiency. For drug release experiments, bGNR@MSN(DOX)-PEG was suspended in PBS at different pH values (5.3 and 7.4) in dialysis tubes of 10 kDa MWCO (molecular weight cut off). At each time point (0.5 h, 3 h, 6 h, 12 h and 24 h), bGNR@MSN(DOX)-PEG solution was irradiated by a NIR laser (0.5 W/cm^2) for 5 min. 0.5 mL dialysis solution was removed after NIR irradiation, and the same volume of PBS buffer was added back in. The amount of DOX was measured by UV—vis spectrometer at a wavelength of 490 nm.

2.5. Cell lines and animal model

4T1 murine breast cancer cells were obtained from the American Type Culture Collection (ATCC, Manassas, VA) and cultured as previously described [36]. Cells were used for in vitro and *in vivo* experiments when they reached ~80% confluence. All animal

studies were conducted under a protocol approved by the University of Wisconsin Institutional Animal Care and Use Committee. 4–5 weeks old female BALB/c mice (Envigo, Indianapolis, IN) were injected with 2×10^6 4T1 cells in the flank (for PET and PA imaging) or shoulder (for photothermal imaging) to generate the 4T1 breast cancer model. The BALB/c mice were used for *in vivo* cancer treatment experiments when the tumor reached 6–8 mm in diameter.

2.6. In vitro photothermal and chemo-photothermal therapy

Murine breast cancer 4T1 cells were cultured at 37 °C and with 5% CO_2 in RPMI 1640 medium supplemented with 10% fetal bovine serum (FBS) and 1% penicillin/streptomycin. Cells were seeded into a 96-well plate with 10^6 cells per well and then incubated for 24 h at 37 °C under 5% CO_2. Different concentration (2 μg/mL, 5 μg/mL and 10 μg/mL) of bGNR@MSN, DOX and bGNR@MSN(DOX)-PEG (with equivalent DOX concentration) in cell culture media solutions were added to the wells and incubated for 4 h before the treatments. For the photothermal therapy and chemo-photothermal therapy, the cells were irradiated by a NIR laser (0.5 W/cm² for 5 min) and followed by further incubation for 12 h. Cell viability was measured using a typical MTT assay.

For trypan blue staining, different concentration (0 μg/mL, 10 μg/mL, 40 μg/mL and 80 μg/mL) of bGNR@MSN-PEG in a PBS solution were added to a cell culture plate containing 4T1 cells and cells were exposed to NIR laser with a power density of 0.5 W/cm² for 5 min and incubated for 4 more hours. Afterward, the cells were stained with 0.4% trypan blue solution for 10 min and washed by with PBS three times. The cell morphology was observed by an inverted optical microscope (Nikon, Eclipse Ti-U, Japan).

2.7. ⁸⁹Zr radiolabeling, PET and PA imaging

Chelator-free ⁸⁹Zr labeling method was used for radiolabeling bGNR@MSN as reported previously by our group [34]. In a typical study, 500 μL of bGNR@MSN-PEG (5 mg) was directly mixed with 1 mCi (or 37 MBq) of ⁸⁹Zr-oxalate at 60 °C for 2 h with constant shaking. The final pH value of the solution was adjusted to 7–8 with Na_2CO_3 (1 M). ⁸⁹Zr labeling yield was monitored by thin layer chromatography (TLC). ⁸⁹Zr-bGNR@MSN-PEG was collected by centrifugation (9000 rpm, 10 min) to remove the free ⁸⁹Zr in the supernatant and finally dispersed in PBS for *in vivo* applications. The labeling yield was monitored and quantified by using TLC.

PET imaging scans of 4T1 tumor-bearing mice (4 mice per group) were performed at various time points post-injection (p.i.) of 4–7 MBq of ⁸⁹Zr-bGNR@MSN(DOX)-PEG via the tail vein, on a microPET/microCT Inveon rodent model scanner (Siemens Medical Solutions USA, Inc.). Detailed procedures for data acquisition, image reconstruction, and region-of-interest (ROI) analysis of the PET imaging data have been reported previously [37]. Quantitative PET data of the 4T1 tumors and major organs were presented as percentage injected dose per gram of tissue (%ID/g).

To validate that the ROI values of PET imaging reflected the radioactivity distribution in mice, ex vivo biodistribution studies were conducted at 24 h p. i. After euthanizing the mice, 4T1 tumors, blood and major organs/tissues were collected and wet weighed. The radioactivity in the tissue or blood was measured by a gamma counter (PerkinElmer) and presented as %ID/g (mean ± SD).

PA imaging was performed by Vevo LAZR Photoacoustic Imaging System (VisualSonics, Inc. Toronto, Canada) with a laser excitation wavelength of 808 nm and a focal depth of 100 mm. 4T1 tumor-bearing mice were scanned before the injection (control) and 24 p. i. with 150 μL bGNR@MSN(DOX)-PEG PBS solution (2 mg/mL).

2.8. In vivo chemo-photothermal therapy

For *in vivo* treatment studies, 4T1 tumor-bearing mice were randomly divided into 5 treatment groups, when the average volume of the tumors reach ~150 mm³: (1) the first group was intravenously (i.v.) injected with PBS solution (150 μL); (2) the second group was i.v. injected with PBS solution (150 μL) and exposed to an 808 nm laser with a power density of 0.5 W/cm² for 5 min at 24 h p. i.; (3) the third group was i.v. injected with bGNR@MSN(DOX)-PEG (2 mg/mL, 150 μL); (4) the fourth group was i.v. injected with bGNR@MSN-PEG in PBS solution (2 mg/mL, 150 μL) and exposed to NIR laser (0.5 W/cm² for 5 min) at 24 h p. i.; (5) the fifth group was i.v. injected with bGNR@MSN(DOX)-PEG in PBS solution (2 mg/mL, 150 μL) and exposed to NIR laser (0.5 W/cm² for 5 min) at 24 h p. i. Tumor temperature and thermal images were monitored and visualized by a FLIRTM E50 camera. Hematoxylin-eosin (H&E) staining of tumors was performed at 24 h after different treatments to compare the therapeutic efficacy. The tumor volumes were recorded every other day for 14 days by caliper measurements.

3. Results and discussion

3.1. bGNR@MSN synthesis and characterizations

The synthetic strategy of bGNR@MSN is shown in Fig. 1. Firstly, CTAC and oleic acid were used as surfactants for highly efficient and
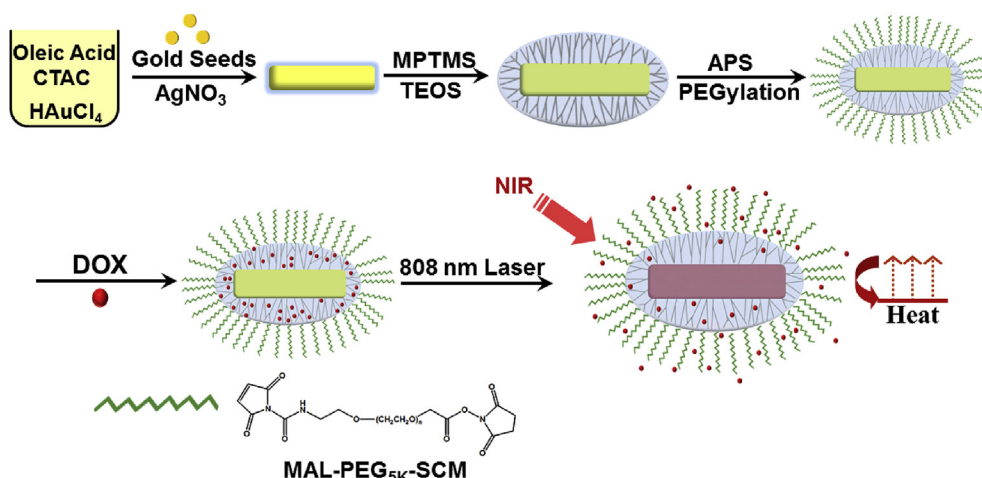

Fig. 1. The scheme showing the synthetic strategy of bGNR@MSN(DOX)-PEG nanoplatforms and possible mechanism of NIR-triggered DOX release.

high yield the synthesis of GNRs by seed-mediated growth method [35]. TEOS was used as silica precursor and the coating process was conducted in an oil-water biphase system. Amino-modification and PEGylation of the surface mesoporous silica layer were then conducted for further biomedical applications. DOX was finally loaded in the mesopores of bGNR@MSN. In our strategy, the 808 nm NIR light was not only used to convert the light to heat to generate local hyperthermia, but also as the external stimulus to accelerate the release of DOX for the synergistic chemo-photothermal therapy.
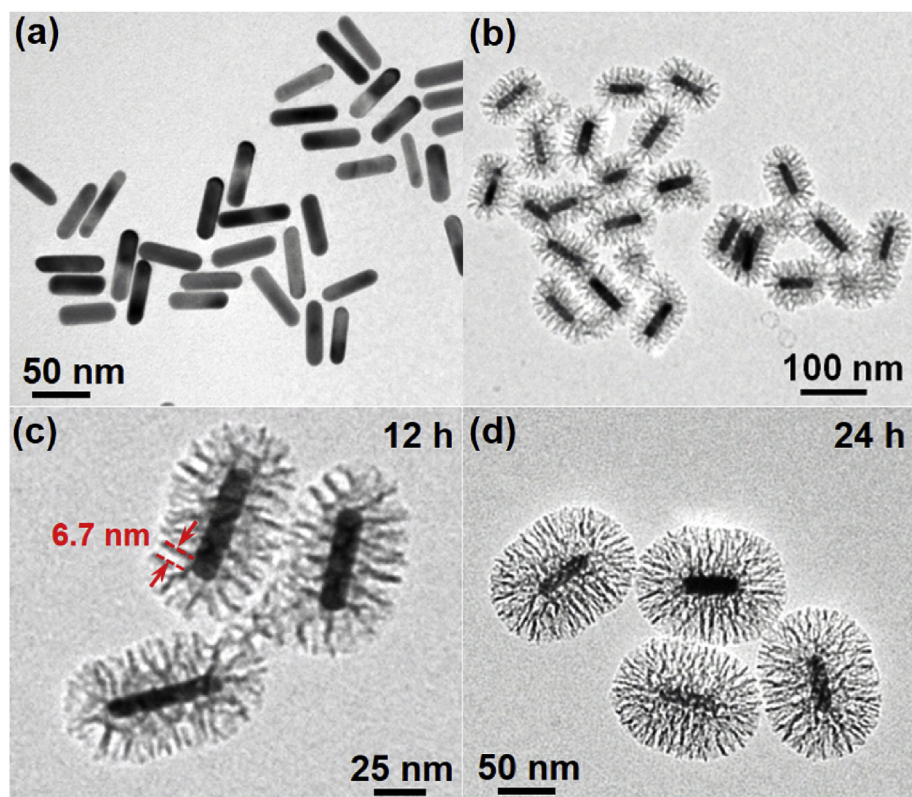
The morphology and structure of GNRs and bGNR@MSN were characterized by TEM as shown in Fig. 2a and b. The average length and width of the obtained surface CTAC-coated GNRs were 60.5 ± 5.3 nm and 16.6 ± 1.9 nm, respectively (Fig. 2a) with an aspect ratio of about 3.7. Inspired by the fabrication of dendritic mesoporous silica nanospheres [26], the surface mesoporous silica coating process of GNRs was achieved in an oil-water biphase reaction system. Cyclohexane was chosen as hydrophobic solvent in the upper oil phase with TEOS (silica precursor), while the lower aqueous phase consists of cationic CTAC as a template and MPTMS promoting the silica assembly on GNRs surface. After coating with mesoporous silica layer, the average length and width of bGNR@MSN increased to 104.6 ± 5.6 nm and 68.6 ± 5.2 nm, respectively. Interestingly, the morphology of as-synthesized bGNR@MSN nanoparticles was observed to be very similar to some prokaryotic bacteria cells (e.g., E. coli), with the outside mesoporous silica layer (Fig. 2c) resembling the bacterial pili. This unique morphology is different from previously reported conventional GNR@MSN synthesized via a one-phase system [11,13,15,16,18]. The thickness of the mesoporous silica layer can be controlled by altering the reaction time. Increasing the time from 12 to 24 h would increase the thickness of MSN layer from

23.5 ± 2.3 nm (Fig. 2c) to 45.1 ± 3.8 nm (Fig. 2d). In this study, bGNR@MSN with shell thickness of 23.5 nm was chosen for subsequent characterization and biomedical applications.
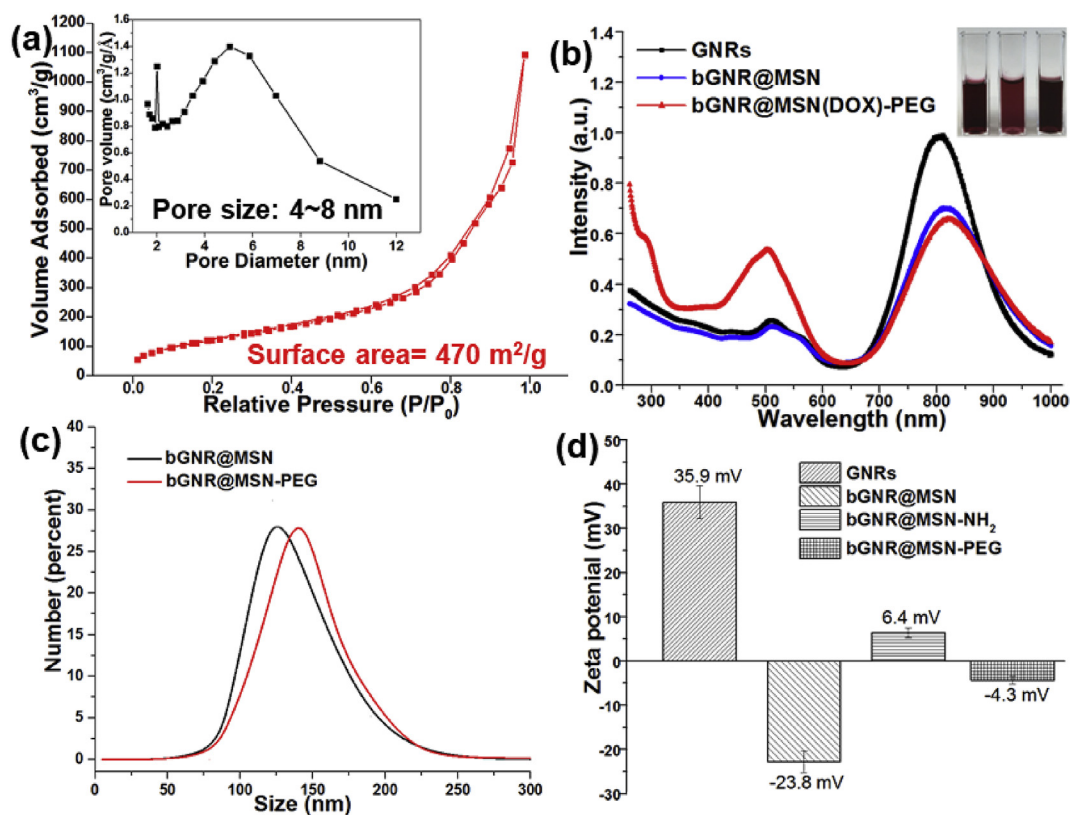
The N$_2$ adsorption-desorption isotherm of bGNR@MSN is shown in Fig. 3a and Fig. S6. The primary pore size distribution (Fig. 3a inset) of bGNR@MSN was in the range of 4–8 nm with a minor peak at 2 nm (average pore size: 5.1 nm). The pore volume and Brunauer-Emmett-Teller (BET) surface area of bGNR@MSN are 1.65 cm^3/g and 470 m^2/g, respectively. The average pore size, pore volume and surface area of bGNR@MSN in this work are higher than most previously reported conventional GNR@MSN (e.g., 2.9 nm, 0.51 cm^3/g and 348 m^2/g, respectively reported by Shen et al. [13]; 2.8 nm, 0.64 cm^3/g and 328 m^2/g, respectively reported by Tang et al. [38]), probably because the silica frameworks on the surface of bGNR@MSN are less dense with lower degree of cross-linking than regular GNR@MSN synthesized in a homogeneous system [26].

GNRs, bGNR@MSN and DOX-loaded bGNR@MSN (i.e., bGNR@MSN(DOX)) were studied by UV–vis absorption spectroscopy (Fig. 3b). CTAC-capped GNRs [35] in this work exhibited a strong longitudinal surface plasmon resonance (SPR) band at around 805 nm, which was red-shifted by about 15 nm after the coating of mesoporous silica layer, possibly due to the fact that local refractive index of silica layer is higher than water [39]. After loading of DOX, an enhanced absorption peak appeared at around 500 nm, which was consistent with previous studies [13].

To prevent aggregation in physiological solution and increase the blood circulation half-life of the final product for enhanced *in vivo* passive tumor targeting efficiency [32], PEGylation process was conducted on the surface of bGNR@MSN. After PEGylation, the average hydrodynamic diameter of bGNR@MSN was further increased from 126.1 nm to 135.9 nm (Fig. 3c) as measured by the

Fig. 2. Morphology and structure of GNRs and bGNR@MSN. (a) TEM image of GNRs; (b) and (c) TEM images of bGNR@MSN with 12 h silica coating time. The red arrows indicate the size (~6.7 nm) of mesopores; (d) TEM image of bGNR@MSN with 24 h silica coating time. (For interpretation of the references to color in this figure legend, the reader is referred to the Web version of this article.)

Fig. 3. (a) Nitrogen adsorption and desorption isotherms and pore size distributions (inset) of bGNR@MSN. (b) UV—vis absorption spectra and photographs (inset, from left to right) of GNRs, bGNR@MSN and bGNR@MSN(DOX). (c) Hydrodynamic size analysis of bGNR@MSN (black line) and bGNR@MSN-PEG (red line) by DLS. (d) Surface zeta potential of GNRs, bGNR@MSN, bGNR@MSN-NH$_2$, bGNR@MSN-PEG. (For interpretation of the references to color in this figure legend, the reader is referred to the Web version of this article.)

dynamic light scattering (DLS). Fig. 3d further showed the change of surface charge after each surface modification. The surface charge of CTAC-capped GNRs in water (pH = 6) were found to be 35.9 ± 3.7 mV, which changed to -23.8 ± 2.5 mV after the coating of silica layers. The surface charge of bGNR@MSN then changed from negative to positive after the surface amination step. The final PEGylated bGNR@MSN was found to be slightly negatively charged (-4.3 ± 0.9 mV) when suspended in PBS solution (pH 7.4).

3.2. Photothermal effect of bGNR@MSN and NIR light triggered DOX release

The photothermal effects of bGNR@MSN at different concentration were compared in Fig. 4a. Dendritic MSNs with similar mesoporous silica structure [26] was synthesized as the control. Upon 808 nm NIR laser irradiation at a power density of 0.25 W/cm^2, the temperature of bGNR@MSN solution (0.5 mg/mL) exceeded 45 °C within 10 min, while the temperature of MSNs solution with a higher concentration (3 mg/mL) and water only increased to 28.5 °C and 26.8 °C, respectively. The photothermal conversion efficiency of bGNR@MSN was calculated following Roper's report [40,41] to be 29.6% (See the Supporting Information for the detailed calculations).

DOX loading was achieved by simply mixing DOX with bGNR@MSN-PEG. The loading efficiency was found to be pH-dependent, as shown in Fig. 4b inset. At pH of 7.4, the average loading efficiency is 40.9% (w/w, 409 mg/g), which decreased to 21.4% (w/w, 214 mg/g) at pH of 5.3 due to higher pH enhanced the hydrophobic interaction between bGNR@MSN and DOX [13]. The DOX loading efficiency of bGNR@MSN-PEG was relatively high

compared with conventional synthesized GNR@MSN-PEG (18.3%, 183 mg/g at pH of 7.4, Fig. S4) and many previously reported GNR@MSN nanocarriers (e.g., 7.0% at pH 7.4 reported by Baek et al. [8]; 25.2% at pH 7.4 reported by Shen et al. [13]; 11.4% at pH 7.4 reported by Liu et al. [15]) owing to the larger pore size (4—8 nm), pore volume (1.65 cm^3/g) and surface area (470 m^2/g).

The release rate of DOX from bGNR@MSN(DOX) depended on the pH of the medium. Under acidic conditions, the release was accelerated because the daunosamine groups of DOX were protonated and the solubility of DOX increased [10]. Since the tumor extracellular environment and intracellular endosomes are acidic [42], accelerated DOX released in acidic conditions could potentially improve the DOX delivery efficiency at the tumor site.

Nevertheless, less than 25% DOX was released from bGNR@MSN(DOX) within 6 h even at the pH of 5.3. Therefore, the photothermal effects of bGNR@MSN were used to further speed up the release of DOX. As shown in Fig. 4b, with a total 15 min NIR irradiation at power density of 0.5 W/cm^2, the cumulative release of DOX increased from 24.5% to 55.5% within 6 h. High DOX loading efficiency as well as pH-sensitive and NIR-triggered release of DOX could potentially make bGNR@MSN one of the most promising candidates for enhanced the chemo-photothermal cancer therapy.

3.3. In vitro photothermal and chemo-photothermal therapy

In order to investigate the in vitro photothermal and chemo-photothermal therapeutic effect of bGNR@MSN nanoplatforms, the cell viability after different treatment methods were measured by MTT viability assays (Fig. 4c) and dead cells staining (Fig. 4d). Without laser and DOX loading, as-synthesized bGNR@MSN had
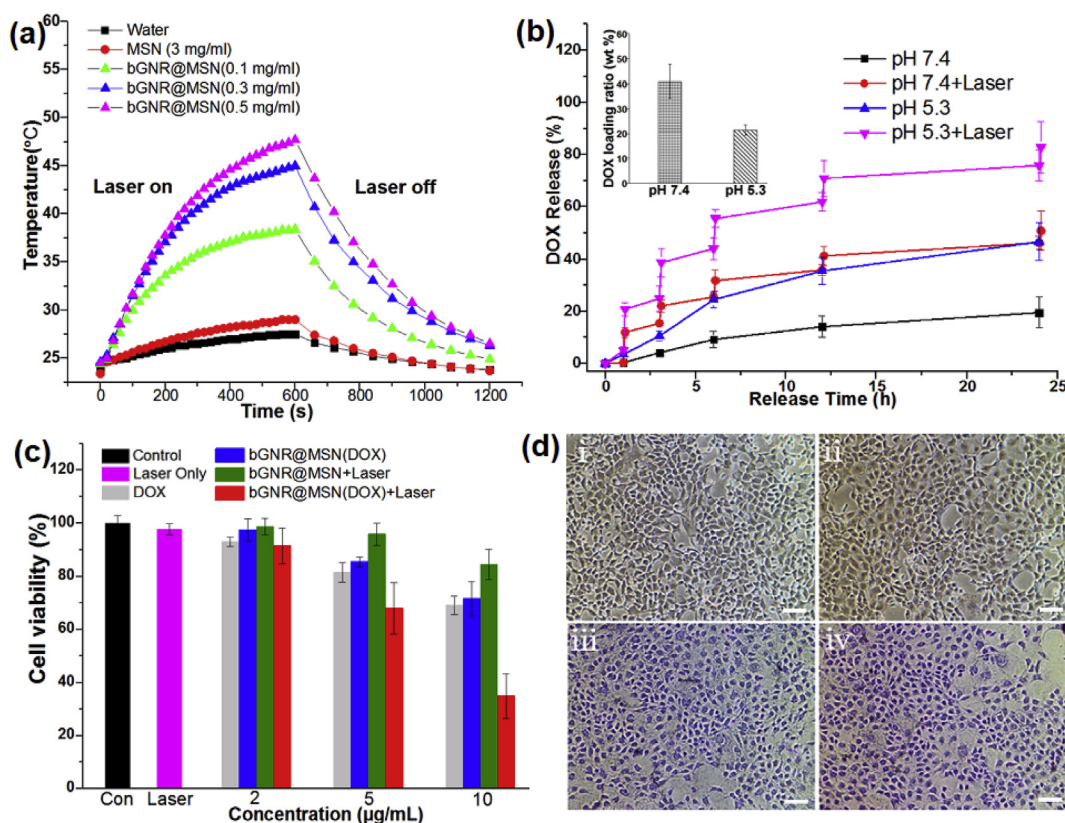
Fig. 4. (a) Photothermal heating curves of GNRs with different concentrations with the 808 nm NIR laser irradiation at a power density of 0.25 W/cm². The MSNs (3 mg/mL) and water were used as control groups. (b) The DOX loading efficiency (inset) and NIR-triggered DOX release under different pH conditions mediated by bGNR@MSN-PEG. (c) Cell viability of 4T1 cells under different in vitro treatment conditions: chemotherapy by DOX (grey) and bGNR@MSN(DOX) (blue); photothermal therapy by bGNR@MSN with NIR laser (0.5 W/cm² for 5min, green); chemo-photothermal therapy by bGNR@MSN(DOX) with NIR laser (0.5 W/cm² for 5min, red). (d) Optical microscopy images of trypan blue-stained cells after incubation with concentration of bGNR@MSN (i: 0 μg/mL; ii: 10 μg/mL; iii: 40 μg/mL; iv: 80 μg/mL) and exposure to the NIR laser (0.5 W/cm² for 5min). Scale bar: 50 μm. (For interpretation of the references to color in this figure legend, the reader is referred to the Web version of this article.)

low cytotoxicity even at a high concentration of 1 mg/mL (Fig. S2). However, the CTAC-capped GNRs killed more than 60% 4T1 cells at the same condition, which highlights the great enhancement of biocompatibility by coating the silica layer. Without the use of nanoparticles, the 808 nm laser alone at the power of 0.5 W/cm² only cause very limited thermal damage to the cells (Fig. 4d(i)).

The efficacy of photothermal therapy alone (0.5 W/cm², 5 min) was low at a low nanoparticles concentration (10 μg/mL) (Fig. 4d(ii)). The thermal therapeutic effects were greatly improved after increasing the concentration of bGNR@MSN (Fig. 4d(iii): 40 μg/mL; (iv): 80 μg/mL) under the same laser illumination condition. For chemotherapy alone, we found that about 31.1% of cells were killed with the presence of 10 μg/mL DOX, as shown in Fig. 4c. In contrast, at the same equivalent DOX concentration, synergistic chemo-photothermal therapy mediated by bGNR@MSN(DOX) killed >65% of cells (Fig. 4c) with an NIR irradiation (0.5 W/cm²,5 min), which showed about 2.3-fold and 4.5-fold enhancement in treatment efficacy over the pure chemotherapy or and photothermal treatment.

3.4. PET imaging and biodistribution studies

The deprotonated silanol groups ($-Si-O^-$) on the surface and inside the mesoporous pores of bGNR@MSN could be used as inherent hard oxygen donors for the stable chelator-free labeling of radioisotope [89]Zr as demonstrated in our previous studies [27,34]. The results of TLC showed that about 68% of chelator-free [89]Zr labeling yield was achieved within the first 30 min incubation at

37 °C. The [89]Zr labeling yield increased over time and reached 95.1% (in 1 g of final radioactive product, about 0.116 mg of [89]Zr was estimated) after 2 h incubation with bGNR@MSN(DOX)-PEG (Fig. 5a).

The PET imaging results of [89]Zr labeled, DOX-loaded bGNR@MSN-PEG (i.e., [89]Zr- bGNR@MSN(DOX)-PEG) at different p.i. time points are shown in Fig. 5b. The quantitative data of PET imaging obtained from region-of-interest (ROI) analysis as shown in Fig. 5c. The in vivo blood circulation time of nanoplatform is highly correlated with the passive tumor targeting efficiency based on EPR (enhanced permeability and retention) effect in leaky tumor models [32]. The surface PEGylation of [89]Zr-bGNR@MSN(DOX)-PEG could reduce the adsorption of serum proteins and prolong the blood circulation time after i.v. injection. The blood circulation half-life of [89]Zr-bGNR@MSN(DOX)-PEG was estimated to be (9.2 ± 0.6) hours which was highly improved after PEGylation compared with the half-life $(1.8 \pm 0.3\,h)$ of [89]Zr-bGNR@MSN(DOX) (Fig. S7). The dominant radioactive signal from mice heart at the first 3 h p.i. clearly indicates the circulation of [89]Zr-bGNR@MSN(DOX)-PEG in mouse blood. Due to the over 100 nm hydrodynamic particle size, [89]Zr-bGNR@MSN(DOX)-PEG tend to non-specifically accumulate to liver and spleen. After 6 h p.i., the [89]Zr-bGNR@MSN(DOX)-PEG were slowly cleared from blood circulation [43]. The average liver uptake of [89]Zr-bGNR@MSN(DOX)-PEG was 26.1 ± 3.0, 26.8 ± 2.7, 26.5 ± 3.5, 24.5 ± 4.1, 24.8 ± 4.2 and 22.2 ± 3.3 %ID/g at 0.5 h, 3 h, 6 h, 12 h, 24 h and 48 h, respectively (n = 4).

[89]Zr-bGNR@MSN(DOX)-PEG slowly accumulated at tumor site over time. The tumor was clearly visible at 12 h p. i. to 48 h p. i.
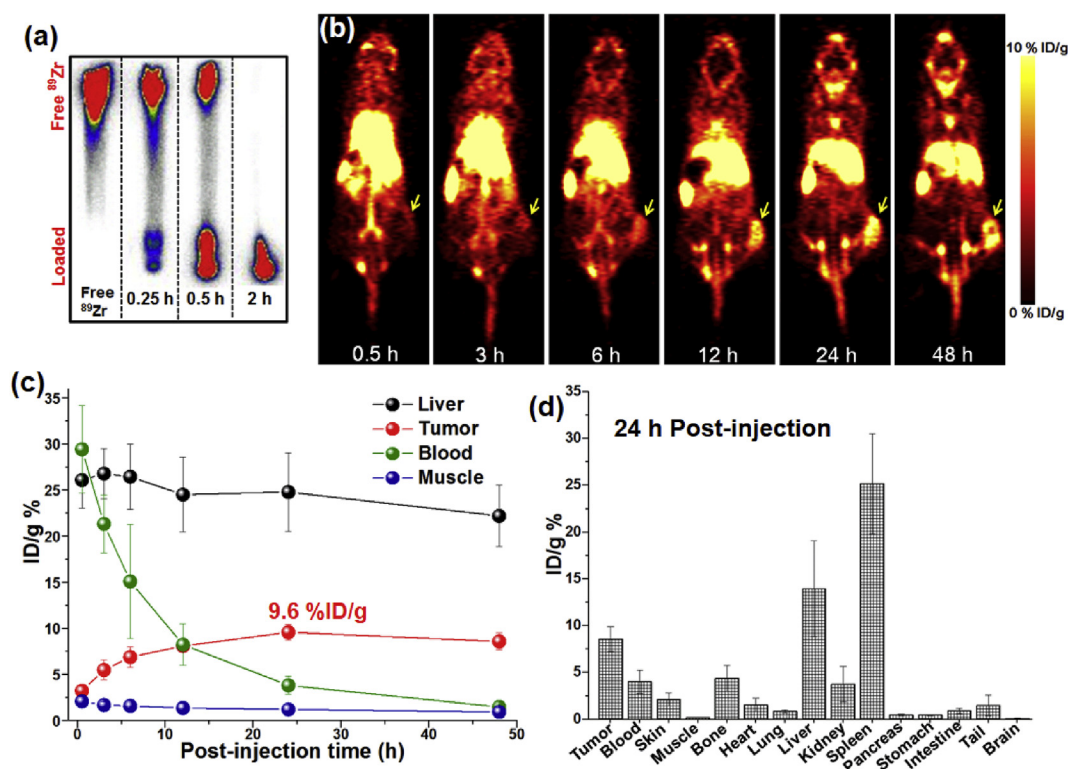
Fig. 5. (a) Autoradiographic images of TLC plates indicating chelator-free radiolabeling of ^{89}Zr-bGNR@MSN(DOX)-PEG at different time points. (b) Serial PET images of 4T1 tumor-bearing mice at different time points p.i. of ^{89}Zr-bGNR@MSN(DOX)-PEG. Tumors are indicated by yellow arrowheads. (c) Time-radioactivity curves of 4T1 tumor, blood, liver and muscle after i.v. injection of ^{89}Zr-bGNR@MSN(DOX)-PEG. (d) Biodistribution studies in 4T1 tumor bearing mice at 24 h p.i. of ^{89}Zr-bGNR@MSN(DOX)-PEG. All data represent 4 mice per group. (For interpretation of the references to color in this figure legend, the reader is referred to the Web version of this article.)

(Fig. 5b). The tumor uptake was 3.3 ± 0.5, 5.5 ± 1.1, 6.9 ± 1.1, 8.1 ± 0.6, 9.6 ± 0.9 and 8.6 ± 0.9 %ID/g at 0.5 h, 3 h, 6 h, 12 h, 24 h and 48 h, respectively (n = 4, Fig. 5c). Remarkably, the passive tumor targeting efficiency of 9.6 %ID/g at 24 h p. i. mediated by ^{89}Zr-

bGNR@MSN(DOX)-PEG was one of the highest tumor uptakes among all previously reported *in vivo* studies of GNRs based nanoplatforms [14,29].

The biodistribution study of ^{89}Zr-bGNR@MSN(DOX)-PEG was
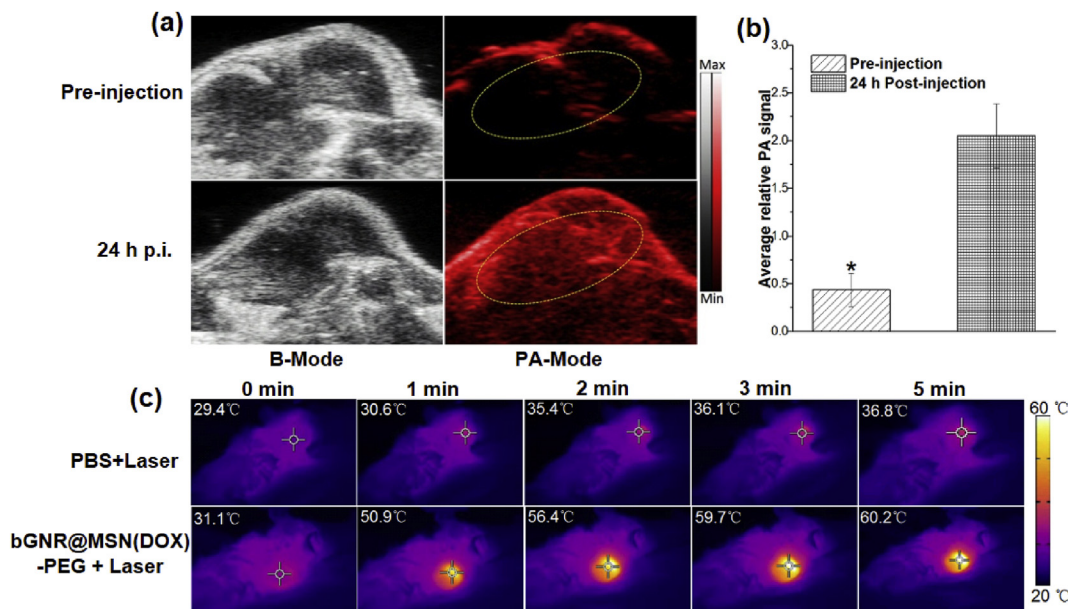
Fig. 6. (a) *In vivo* PA imaging of 4T1 tumor-bearing mice at before and 24 h post-i. v. injection of bGNR@MSN(DOX)-PEG. (b) Quantitative ROI analysis results of photoacoustic signal within the yellow circles in PA images. (c) Photothermal images of 4T1 tumor-bearing mice under 808 nm NIR laser irradiation after 24 h of i. v. injection of PBS (150 μL) or bGNR@MSN(DOX)-PEG (150 μL, 2 mg/mL) taken by a thermal camera. (For interpretation of the references to color in this figure legend, the reader is referred to the Web version of this article.)

carried out at 24 h p. i. to validate the results from the PET imaging study. As shown in Fig. 5d, the biodistribution data and quantitative PET data matched well. The average tumor uptake was 8.6 %ID/g at 24 h p. i. The average spleen and liver uptake at 24 h p. i. were 25.1 ± 5.3 and 13.9 ± 5.1 %ID/g, respectively, as expected for i.v. injected nanoparticles with hydrodynamic diameters >10 nm, that are sequestered by the organs of the reticulo-endothelial system.

3.5. PA imaging of bGNR@MSN(DOX)-PEG

PA imaging with high spatial resolution, noninvasive deep tissue penetration and short scan time is a good complementary imaging modality for PET [32]. bGNR@MSN(DOX)-PEG nanoplatforms with high absorption in NIR range could be promising contrast agents for in vivo PA imaging. As shown in Fig. 6a and 24 h after i. v. injection of bGNR@MSN(DOX)-PEG, significant photoacoustic signal was observed from the tumor, which was clearly stronger than pre-injection signal. The quantitative ROI analysis results of photo-acoustic signal within the yellow circles (Fig. 6a) are shown in Fig. 6b. The signal at 24 p. i. time point is 4.7-fold stronger than pre-injection.

Considering that PA imaging displays the actual location of the bGNR@MSN-PEG nanoparticles owing to the photoacoustic signals from GNRs, dual-modality PET/PA imaging further confirmed the enhanced accumulation of bGNR@MSN-PEG nanoplatforms in tumor, thereby providing multi-dimensional and more accurate information for the subsequent in vivo chemo-photothermal tumor therapy. Moreover, good correlation between the PET and PA images, further confirmed the excellent radiostability of [89]Zr-bGNR@MSN(DOX)-PEG, validating their use as multimodal imaging agents.

3.6. In vivo chemo-photothermal therapy with NIR light

In vivo photothermal imaging was performed by 808 nm NIR laser irradiation, 24 h after i. v. injection of bGNR@MSN(DOX)-PEG in 4T1 tumor-bearing mice. The thermal images of tumor were visualized by a thermal camera, as shown in Fig. 6c. During the laser irradiation at a power density of 0.5 W/cm^2, the tumor temperature increased rapidly and exceeded over 50 °C within 1 min and
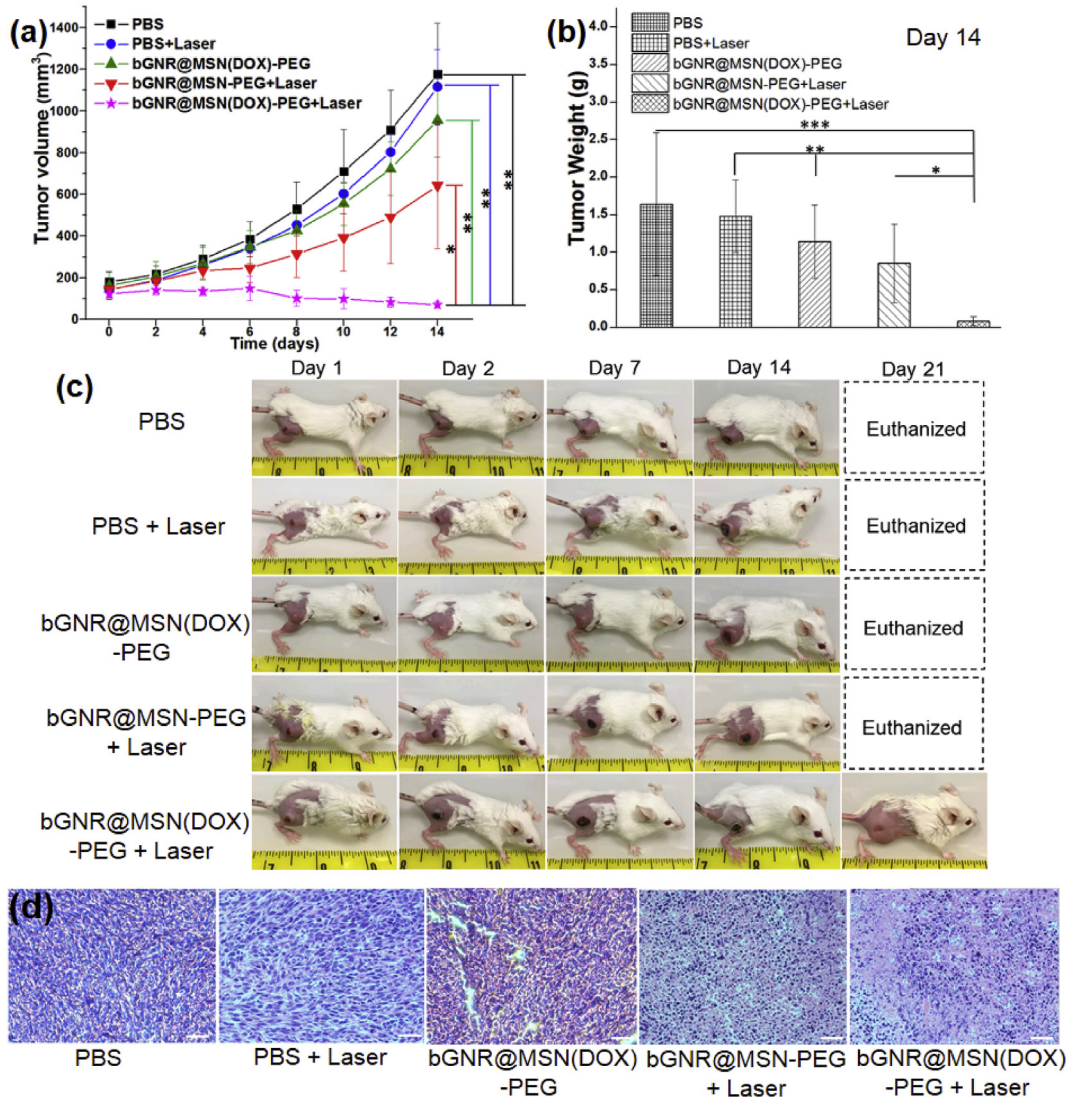
Fig. 7. (a) 4T1 tumor growth profiles after different treatments (n = 4). (b) Weight of dissected 4T1 tumors at Day 14 after different treatments (n = 4, *P < 0.05, **P < 0.01, ***P < 0.001). (c) Representative photographs of mice before various treatments (Day 1) and after the treatments (Day 2, Day 7, Day 14 and Day 21). The unit of the ruler is inch. (d) H&E staining of tumor sections 24 h after different treatments. Scale bar: 100 μm.

reaching 60.2 °C at the end of irradiation, which caused instantaneous and irreversible cell death in the tumors [13]. In contrast, without the injection of nanoplatforms, the temperate increased slowly and only reached 36.8 °C after 5 min laser irradiation (Fig. 6c).

Taking advantages of excellent photothermal effects *in vivo* and NIR-triggered drug release, the chemo-photothermal treatments were performed when the average volume of 4T1 tumors reach ~150 mm^3 on the flank of BALB/c mice (Fig. 7b). 24 h after i. v. injection of bGNR@MSN(DOX)-PEG, the tumor was irradiated with NIR laser (0.5 W/cm^2 for 5 min). Four other groups including untreated mice group (PBS only), laser irradiation only group, injection of bGNR@MSN(DOX)-PEG group (chemotherapy, no laser) and injection of bGNR@MSN-PEG with laser irradiation group (photothermal therapy, no DOX) were used as control groups. As shown in Fig. 7a, the tumors in the untreated group and laser irradiation only group grew rapidly. There was no statistically significant difference in final tumor sizes between the two groups indicating that tumor growth was not affected by the laser irradiation alone. Simply laser-triggered hyperthermia induced by bGNR@MSN-PEG (photothermal therapy group) exhibited better anti-tumor effects (average tumor volume and weight at Day 14: 641.6 mm^3 and 1.14 g, respectively) than simple DOX-delivery (average tumor volume and weight at Day 14: 956.1 mm^3 and 0.85 g, respectively), although very limited antitumor effects were shown in those two groups. Remarkably, the tumor growth in chemo-photothermal treatment group was completely inhibited and the tumor volume and weight (69.8 mm^3 and 0.08 g, respectively) at Day 14 showed statistical difference (p < 0.01) with other 4 groups (Fig. 7a and b). 75% of the established 4T1 tumors in this group were eradicated completely by Day 21 as shown in the digital photographs of Fig. 7c without subsequent recurrence for six weeks (Fig. S3). The significant enhancement in therapeutic efficacy observed here by combination chemo-photothermal treatment can be explained as follows: (1) while only a limited amount of DOX is released from the nanoplatforms at the physiological temperature, the release could be greatly enhanced under hyperthermia when exposed to NIR light; (2) local hyperthermia (~60 °C) itself induces rapid and irreversible cancer cell death; and (3) potential enhancement in cytotoxicity by DOX at elevated temperatures, as reported previously [44].

The hematoxylin and eosin (H&E) staining was used to investigate the morphology and apoptosis in tumor tissues 24 h after different treatments as shown in Fig. 7d. The H&E staining results in chemo-photothermal therapy group showed most tumor cells damage among all five treatment groups which further confirmed results of tumor size and weight measurements in Fig. 7a and b. And the H&E stained images of major organs (heart, liver, kidney, spleen and lung) showed no noticeable organ damage or inflammatory lesions over 30 days (Fig. S9), suggesting the low *in vivo* toxicity of bGNR@MSN(DOX)-PEG. Overall, the findings in this work indicate that the combination of photothermal therapy and chemotherapy by bGNR@MSN(DOX)-PEG nanoplatforms results in great enhancement in tumor treatment efficacy, over and above the therapeutic effects demonstrated by single modalities alone.

4. Conclusions

In summary, bacteria-like mesoporous silica-coated gold nanorods were successfully synthesized with significant enlarged pore size and surface area. After PEGylation, high efficient DOX loading and chelator-free ^{89}Zr radiolabeling, ^{89}Zr-bGNR@MSN(DOX)-PEG nanoplatforms served as both the contrast agents and therapeutic agents for PET and PA imaging-guided chemo-photothermal cancer therapy *in vivo*. PET imaging showed that bGNR@MSN(DOX)-PEG can passively target to tumor area with a high tumor accumulation (~10 %ID/g) based on EPR effect. The PA imaging results also confirmed the enhanced accumulation of bGNR@MSN(DOX)-PEG at the tumor site. Significantly enhanced therapeutic effects were achieved by bGNR@MSN(DOX)-PEG treatment under NIR laser irradiation when compared with single chemotherapy or photothermal therapy, which shows the promising and potential applications in future cancer diagnosis and therapy.

Notes

Acknowledgment

Appendix A. Supplementary data

Supplementary data related to this article can be found at https://doi.org/10.1016/j.biomaterials.2018.02.043.

References

[1] S.C. Nguyen, Q. Zhang, K. Manthiram, X. Ye, J.P. Lomont, C.B. Harris, H. Weller, A.P. Alivisatos, Study of heat transfer dynamics from gold nanorods to the environment via time-resolved infrared spectroscopy, ACS Nano 10 (2016) 2144–2151.

[2] S.F. Tan, U. Anand, U. Mirsaidov, Interactions and attachment pathways between functionalized gold nanorods, ACS Nano 11 (2017) 1633–1640.

[3] C. Xu, D. Yang, L. Mei, B. Lu, L. Chen, Q. Li, H. Zhu, T. Wang, Encapsulating gold nanoparticles or nanorods in graphene oxide shells as a novel gene vector, ACS Appl. Mater. Interfaces 5 (2013) 2715–2724.

[4] N.D. Burrows, W. Lin, J.G. Hinman, J.M. Dennison, A.M. Vartanian, N.S. Abadeer, E.M. Grzincic, L.M. Jacob, J. Li, C.J. Murphy, Surface chemistry of gold nanorods, Langmuir 32 (2016) 9905–9921.

[5] X. Sun, X. Huang, X. Yan, Y. Wang, J. Guo, O. Jacobson, D. Liu, L.P. Szajek, W. Zhu, G. Niu, Chelator-free 64Cu-integrated gold nanomaterials for positron emission tomography imaging guided photothermal cancer therapy, ACS Nano 8 (2014) 8438–8446.

[6] X. Huang, I.H. El-Sayed, W. Qian, M.A. El-Sayed, Cancer cell imaging and photothermal therapy in the near-infrared region by using gold nanorods, J. Am. Chem. Soc. 128 (2006) 2115–2120.

[7] S. Wang, X. Zhao, S. Wang, J. Qian, S. He, Biologically inspired polydopamine capped gold nanorods for drug delivery and light-mediated cancer therapy, ACS Appl. Mater. Interfaces 8 (2016) 24368–24384.

[8] S. Baek, R.K. Singh, T.H. Kim, J.W. Seo, U.S. Shin, W. Chrzanowski, H.W. Kim, Triple hit with drug carriers: pH- and temperature-responsive theranostics for multimodal chemo- and photothermal therapy and diagnostic applications, ACS Appl. Mater. Interfaces 8 (2016) 8967–8979.

[9] E. Ju, Z. Li, Z. Liu, J. Ren, X. Qu, Near-infrared light-triggered drug-delivery vehicle for mitochondria-targeted chemo-photothermal therapy, ACS Appl. Mater. Interfaces 6 (2014) 4364–4370.

[10] C. Xu, D. Yang, L. Mei, Q. Li, H. Zhu, T. Wang, Targeting chemophotothermal therapy of hepatoma by gold nanorods/graphene oxide core/shell nanocomposites, ACS Appl. Mater. Interfaces 5 (2013) 12911–12920.

[11] X. Yang, X. Liu, Z. Liu, F. Pu, J. Ren, X. Qu, Near-infrared light-triggered, targeted drug delivery to cancer cells by aptamer gated nanovehicles, Adv. Mater. 24 (2012) 2890–2895.

[12] C. Yu, J. Irudayaraj, Multiplex biosensor using gold nanorods, Anal. Chem. 79 (2007) 572–579.

[13] S. Shen, H. Tang, X. Zhang, J. Ren, Z. Pang, D. Wang, H. Gao, Y. Qian, X. Jiang, W. Yang, Targeting mesoporous silica-encapsulated gold nanorods for chemo-photothermal therapy with near-infrared radiation, Biomaterials 34 (2013) 3150–3158.

[14] C. Qin, J. Fei, A. Wang, Y. Yang, J. Li, Rational assembly of a biointerfaced core@shell nanocomplex towards selective and highly efficient synergistic photothermal/photodynamic therapy, Nanoscale 7 (2015) 20197–20210.

[15] J. Liu, C. Detrembleur, D. Pauw-Gillet, S. Mornet, C. Jérôme, E. Duguet, Gold nanorods coated with mesoporous silica shell as drug delivery system for remote near infrared light-activated release and potential phototherapy,

Small 11 (2015) 2323—2332.

[16] Y. Liu, M. Xu, Q. Chen, G. Guan, W. Hu, X. Zhao, M. Qiao, H. Hu, Y. Liang, H. Zhu, Gold nanorods/mesoporous silica-based nanocomposite as theranostic agents for targeting near-infrared imaging and photothermal therapy induced with laser, Int. J. Nanomed. 10 (2015) 4747—4761.

[17] A.M. Alkilany, P.K. Nagaria, C.R. Hexel, T.J. Shaw, C.J. Murphy, M.D. Wyatt, Cellular uptake and cytotoxicity of gold nanorods: molecular origin of cytotoxicity and surface effects, Small 5 (2009) 701—708.

[18] Y. Li, T. Wen, R. Zhao, X. Liu, T. Ji, H. Wang, X. Shi, J. Shi, J. Wei, Y. Zhao, Localized electric field of plasmonic nanoplatform enhanced photodynamic tumor therapy, ACS Nano 8 (2014) 11529—11542.

[19] T. Niidome, M. Yamagata, Y. Okamoto, Y. Akiyama, H. Takahashi, T. Kawano, Y. Katayama, Y. Niidome, PEG-modified gold nanorods with a stealth character for in vivo applications, J. Contr. Rel. 114 (2006) 343—347.

[20] H.Y. Chen, S. Abraham, J. Mendenhall, S.C. Delamarre, K. Smith, I. Kim, C.A. Batt, Encapsulation of single small gold nanoparticles by diblock copolymers, ChemPhysChem 9 (2008) 388—392.

[21] N.S. Abadeer, M.R. Brennan, W.L. Wilson, C.J. Murphy, Distance and plasmon wavelength dependent fluorescence of molecules bound to silica-coated gold nanorods, ACS Nano 8 (2014) 8392—8406.

[22] Z. Liu, X. Liu, X. Ran, E. Ju, J. Ren, X. Qu, Single-layer tungsten oxide as intelligent photo-responsive nanoagents for permanent male sterilization, Biomaterials 69 (2015) 56—64.

[23] Z. Liu, X. Liu, Y. Du, J. Ren, X. Qu, Using plasmonic copper sulfide nanocrystals as smart light-driven sterilants, ACS Nano 9 (2015) 10335—10346.

[24] Z. Liu, J. Liu, R. Wang, Y. Du, J. Ren, X. Qu, An efficient nano-based theranostic system for multi-modal imaging-guided photothermal sterilization in gastrointestinal tract, Biomaterials 56 (2015) 206—218.

[25] Z. Zhang, C. Liu, J. Bai, C. Wu, Y. Xiao, Y. Li, J. Zheng, R. Yang, W. Tan, Silver nanoparticle gated, mesoporous silica coated gold nanorods (AuNR@MS@AgNPs): low premature release and multifunctional cancer theranostic platform, ACS Appl. Mater. Interfaces 7 (2015) 6211—6219.

[26] D. Shen, J. Yang, X. Li, L. Zhou, R. Zhang, W. Li, L. Chen, R. Wang, F. Zhang, D. Zhao, Biphase stratification approach to three-dimensional dendritic biodegradable mesoporous silica nanospheres, Nano Lett. 14 (2014) 923—932.

[27] S. Goel, F. Chen, S. Luan, H.F. Valdovinos, S. Shi, S.A. Graves, F. Ai, T.E. Barnhart, C.P. Theuer, W. Cai, Engineering intrinsically zirconium-89 radiolabeled self-destructing mesoporous silica nanostructures for in vivo biodistribution and tumor targeting studies, Adv. Sci. 3 (2016), 1600122.

[28] M.N. Sanz-Ortiz, K. Sentosun, S. Bals, L.M. Liz-Marzán, Templated growth of surface enhanced Raman scattering-active branched gold nanoparticles within radial mesoporous silica shells, ACS Nano 9 (2015) 10489—10497.

[29] X. Sun, W. Cai, X. Chen, Positron emission tomography imaging using radiolabeled inorganic nanomaterials, Acc. Chem. Res. 48 (2015) 286—294.

[30] F. Chen, P.A. Ellison, C.M. Lewis, H. Hong, Y. Zhang, S. Shi, R. Hernandez, M.E. Meyerand, T.E. Barnhart, W. Cai, Chelator-free synthesis of a dual-modality PET/MRI agent, Angew. Chem. Int. Ed. 52 (2013) 13319—13323.

[31] Y. Liu, L. Nie, X. Chen, Photoacoustic molecular imaging: from multiscale biomedical applications towards early-stage theranostics, Trends Biotechnol. 34 (2016) 420—433.

[32] C. Xu, S. Shi, L. Feng, F. Chen, S.A. Graves, E.B. Ehlerding, S. Goel, H. Sun, C.G. England, R.J. Nickles, Long circulating reduced graphene oxide—iron oxide nanoparticles for efficient tumor targeting and multimodality imaging, Nanoscale 8 (2016) 12683—12692.

[33] Y. Huang, S. He, W. Cao, K. Cai, X.-J. Liang, Biomedical nanomaterials for imaging-guided cancer therapy, Nanoscale 4 (2012) 6135—6149.

[34] F. Chen, S. Goel, H.F. Valdovinos, H. Luo, R. Hernandez, T.E. Barnhart, W. Cai, In vivo integrity and biological fate of chelator-free zirconium-89-labeled mesoporous silica nanoparticles, ACS Nano 9 (2015) 7950—7959.

[35] X. Ye, Y. Gao, J. Chen, D.C. Reifsnyder, C. Zheng, C.B. Murray, Seeded growth of monodisperse gold nanorods using bromide-free surfactant mixtures, Nano Lett. 13 (2013) 2163—2171.

[36] S. Shi, K. Yang, H. Hong, H.F. Valdovinos, T.R. Nayak, Y. Zhang, C.P. Theuer, T.E. Barnhart, Z. Liu, W. Cai, Tumor vasculature targeting and imaging in living mice with reduced graphene oxide, Biomaterials 34 (2013) 3002—3009.

[37] F. Chen, H. Hong, Y. Zhang, H.F. Valdovinos, S. Shi, G.S. Kwon, C.P. Theuer, T.E. Barnhart, W. Cai, In vivo tumor targeting and image-guided drug delivery with antibody-conjugated, radiolabeled mesoporous silica nanoparticles, ACS Nano 7 (2013) 9027—9039.

[38] H. Tang, S. Shen, J. Guo, B. Chang, X. Jiang, W. Yang, Gold nanorods@ mSiO 2 with a smart polymer shell responsive to heat/near-infrared light for chemophototothermal therapy, J. Mater. Chem. 22 (2012) 16095—16103.

[39] J.V. Jokerst, M. Thangaraj, P.J. Kempen, R. Sinclair, S.S. Gambhir, Photoacoustic imaging of mesenchymal stem cells in living mice via silica-coated gold nanorods, ACS Nano 6 (2012) 5920—5930.

[40] D.K. Roper, W. Ahn, M. Hoepfner, Microscale heat transfer transduced by surface plasmon resonant gold nanoparticles, J. Phys. Chem. C 111 (2007) 3636—3641.

[41] W. Zhang, G. Deng, B. Li, X. Zhao, T. Ji, G. Song, Z. Xiao, Q. Cao, J. Xiao, X. Huang, Degradable rhenium trioxide nanocubes with high localized surface plasmon resonance absorbance like gold for photothermal theranostics, Biomaterials 159 (2018) 68—81.

[42] Y. Wang, K. Wang, J. Zhao, X. Liu, J. Bu, X. Yan, R. Huang, Multifunctional mesoporous silica-coated graphene nanosheet used for chemo-photothermal synergistic targeted therapy of glioma, J. Am. Chem. Soc. 135 (2013) 4799—4804.

[43] M. Yu, J. Zheng, Clearance pathways and tumor targeting of imaging nanoparticles, ACS Nano 9 (2015) 6655—6674.

[44] O. Tacar, P. Sriamornsak, C.R. Dass, Doxorubicin: an update on anticancer molecular action, toxicity and novel drug delivery systems, J. Pharm. Pharmacol. 65 (2013) 157—170.